Mechanisms underlying enhanced strength-ductility combinations in TRIP/TWIP Ti-12Mo alloy engineered via isothermal omega precipitation

Bingnan Qian, Srinivas Aditya Mantri, Sriswaroop Dasari, Jinyong Zhang, Lola Lilensten, Fan Sun, Philippe Vermaut, Rajarshi Banerjee, Frédéric Prima

▶ To cite this version:

Bingnan Qian, Srinivas Aditya Mantri, Sriswaroop Dasari, Jinyong Zhang, Lola Lilensten, et al.. Mechanisms underlying enhanced strength-ductility combinations in TRIP/TWIP Ti-12Mo alloy engineered via isothermal omega precipitation. Acta Materialia, 2023, 245, pp.118619. 10.1016/J.ACTAMAT.2022.118619 . hal-04333966

HAL Id: hal-04333966
https://hal.science/hal-04333966

Submitted on 10 Dec 2023

Mechanisms underlying enhanced strength-ductility combinations in TRIP/TWIP Ti-12Mo alloy engineered via isothermal omega precipitation

(*This is the revised version of 11.2022 – before acceptation in Acta Materialia*)

Bingnan Qian [a,b], Srinivas Aditya Mantri [c,d], Sriswaroop Dasari [c,d], Jinyong Zhang [e,f], Lola Lilensten [a], Fan Sun [a*], Philippe Vermaut [a,g], Rajarshi Banerjee [e,f], Frédéric Prima [a]

a. PSL University, Chimie ParisTech, CNRS, Institut de Recherche de Chimie Paris, Paris, France 75005

b. Department of Mechanical and Energy Engineering, Southern University of Science and Technology, Shenzhen People's Republic of China 518055

c. Department of Materials Science and Engineering, University of North Texas, Denton, United States, TX 76207

d. Center for Advanced Research and Technology, University of North Texas, Denton, United States, TX

e. School of Material Science and Engineering, China University of Mining and Technology, Xuzhou, People's Republic of China 221008

f. State Key Laboratory of Solidification Processing, Northwestern Polytechnical University, Xi'an, People's Republic of China 710072

g. Sorbonne Universities, UPMC University Paris, UFR926, Paris, France 75006

Corresponding author Email: fan.sun@chimieparistech.psl.eu (Fan Sun)

Keywords: Titanium alloy; Deformation twinning; Phase transformation; Omega phase; Mechanical properties.

Abstract

β Ti-alloys can achieve a high strain-hardening rate and tensile ductility by taking advantage of transformation induced plasticity (TRIP) and twinning-induced plasticity (TWIP) effects. While nano-precipitation of isothermal ω (ω_{iso}) can have a substantial strengthening effect in these alloys, it usually has a detrimental effect on ductility leading to embrittlement. To overcome the above problem, this work proposes as a novel strategy based on coupling of ω_{iso} formation and mechanical twinning/martensitic transformation to enhance the strength while preserving good ductility in case of the TRIP/TWIP Ti-12Mo alloy. An unprecedented combination of tensile properties, yield stress at 865MPa (80% higher than classic Ti-12Mo) with uniform elongation of 0.35, are recorded after 200°C aging for 60s. Higher yielding stress (990MPa) is achieved when increasing the aging duration to 150s where mechanical twinning is still active. *In-situ* investigations under traction/heating, and atom probe tomography are performed to clarify the ω_{iso} formation process and the interactions between ω phase and the operating deformation mechanisms, i.e. mechanical {332}<113> twinning, $\beta \rightarrow \alpha''$ martensitic transformation and dislocation glide. The early stages of formation of ω_{iso} precipitates, mediated via Mo partitioning at low aging temperature, and its consequent impact on the deformation mechanisms operative in the β matrix has been characterized. The transformation partition mapping method, based on statistical electron backscatter diffraction characterization developed in our previous work, is employed to individually assess the evolution of the critical resolved shear stresses of each operating deformation mechanism as a function of the ω_{iso} nucleation.

1. Introduction

A new family of metastable β titanium alloys with twinning induced plasticity (TWIP) and transformation induced plasticity (TRIP) effects have been investigated extensively, leading to great potential applications, thanks to their high specific strength, excellent corrosion resistance, and biocompatibility [1-6]. These TRIP/TWIP Ti-alloys possess a wide range of mechanical properties due to their different combinable deformation mechanisms, mainly including {332}<113>$_\beta$ twinning (hereafter called 332T), {112}<111>$_\beta$ twinning, stress-induced martensite (SIMα″), and dislocation glide. Some research has been devoted to 332T and SIMα″, about the microstructure/mechanical property relationships [1-6], the hierarchical structure [5], the interfaces/dislocation interaction [4], the modelling of 332T [7] and the crystallography of transformation products via theoretical and experimental methods [8]. In that frame, the TRIP/TWIP Ti-12 Mo (wt.%) binary alloy has been investigated thoroughly regarding mechanical properties, microstructures, thermomechanical treatments, failure mechanisms, twinning and martensite transformation pathways via various methods including controlled deformation conditions, in-situ microcopies and quantitative micro-analysis [1,2,9,10]. The growing knowledge from these researches has allowed to clarify the alloy's details at multi-length scales and is now indispensable for a further microstructural engineering work to explore the precipitation strengthening in cooperation with TRIP/TWIP effects. After being quenched from the high-temperature β field, ω phase, as the quenched-in nano-precipitates (5nm in average size at 15 vol%) [11], is known to form in the retained metastable β phase via a displacive phase transformation. The quenched-in ω phase exhibits an hexagonal structure with fully collapsed {111} β plane [11] with orientation relationships $(0001)_\omega//(111)_\beta$, it is usually referred to as athermal omega (ω_{ath}) phase. The ω_{iso} phase forms via a diffusion-controlled precipitation process usually at temperature range 150°C - 475°C, resulting in uniformly dispersed ω precipitates in the β matrix [11]. ω_{iso} is well-known for its sharp strengthening effect in β Ti alloys but usually accompanied with detrimental embrittlement due to its strong influence on the operation of deformation mechanisms [28]. Many previous studies have been conducted to understand the interactions between ω_{iso} phase and deformation mechanisms, i.e. SIMα″, twinning, and dislocation slip. Chen et al. [14] suggested that the structure evolution of ω phase during aging at 300°C controls the deformation mechanism transformation of twinning-to-slip in Ti-Mo alloy [29]. Sun et al. [9] reported that low temperature aging treatments for short time periods could enhance the yield strength while maintaining the ductility in ω containing Ti-12Mo alloy. In addition, Lai et al. also reported that the mechanical behavior could be significantly affected by ω phase precipitation due to the suppression of TRIP and TWIP effects by ω particles [15]. First principle calculations [16] suggest that the ω strengthening and embrittlement effect in Ti-Mo alloy result from the high slip energy barriers in the ω phase when compared to those in the β phase. The depletion of Mo of ω phase leads to increases of energy barriers, as well as shear modulus [17,19], resulting in considerable strengthening effect but embrittlement after aging treatments. Therefore, both the elastic effect and chemical effect (Mo enrichment) causing by ω phase leads to the suppression of TRIP and TWIP effect.

Based on the above knowledge, the strategy employed in this work to overcome the ω embrittlement is to preserve the TRIP and TWIP activities in a balance with ω_{iso} precipitation. The analysis of precipitation process and its influence on each operative mechanism is of great importance to achieve a metastable β matrix strengthened by nano ω_{iso} precipitates at a suitable volume fraction where SIM α″, mechanical twinning, and dislocation slip keep being operational simultaneously in the polycrystalline aggregate. As suggested at the end of our short communication on omega strengthening strategy using low-temperature aging [9], this work follows to understand the mechanism of transition from ω_{ath} to ω_{iso} precipitates and its consequent influences on SIM α″, 332-type mechanical twinning and dislocation slip.

The grain-resolved activation between SIM α″ and twinning both depends on several material factors such as β phase stability [1-4], grain orientation (Schmid factor and texture) [10], and micro-stress distribution in the aggregate [5]. A phenomenological method to deal with such multi-factorial problems has been developed, as the preliminary study of the current one [10]. This approach allows a quantification of the differences between different TRIP/TWIP states. The method is based on matching between experimental transformation partition maps (TPM) and theoretical TPMs to determine the Schmid factor threshold (minimum necessary for activation) of each deformation mechanism [10]. The SF thresholds can be used as indicators of TRIP and TWIP activities with better practical accessibility in metastable BCC alloys than others phase stability indicators such as temperature M_s/M_d (Temperature M_s, martensite start temperature; temperature M_d, the temperature above which no phase transformation occurs by plastic deformation).

Therefore, the present work aims to clarify, based on the current knowledge, the relationship between ω_{iso} formation and the evolution of deformation mechanisms (TRIP/TWIP/dislocation slip) in Ti-12Mo. Short time isothermal aging (at 200°C) has been employed to develop ω_{iso} precipitates with marginal changes in composition, as compared to the quenched-in ω_{ath} precipitates. The early stages of formation of ω_{iso} precipitates has been tracked via a combination of atom probe tomography (APT) and TEM. The influence of these precipitates (at their different stages of formation) on the balance between TRIP, TWIP and dislocation slip deformation mechanisms is discussed based on results of *in-situ* EBSD and TEM observations under tensile loading. The grain-resolved Schmid factor statistics using TPM method has also been employed to determine the operative deformation mechanism. Based on these results, we demonstrate that ω_{iso} precipitates can, under some specific aging conditions, be used as a design strategy for unprecedented strength-ductility combinations in metastable beta Ti alloys.

2. Materials and methods

The Ti-12Mo (wt. %) ingot is fabricated by vacuum arc-melting using high purity Ti (99.6%) and Mo (99.98%) metals. The alloy is melted at least five times under a high purity argon atmosphere. The ingot is annealed in vacuum tubular furnace under 2.0 x 10^{-4} Pa at 900°C for 1.8 ks, followed by water quenching. The quenched ingot is cold rolled to 0.5mm sheets, corresponding to reduction rate of 95%. The cold-rolled sheets are recrystallized at 900°C under high vacuum (2.0×10^{-4} Pa) for 60 s then quenched in water to limit the grain size to 20-30 μm in the fully recrystallized alloy. The studied alloy is thereafter called fine-grain Ti-12Mo to differentiate from classic Ti-12Mo with grain size at about 100 μm (called coarse-grain Ti-12Mo) used in previous studies. Tensile test samples with gauge dimensions 40 mm × 4 mm × 0.5 mm, are immersed into oil bath (SilOil with 300°C boiling point, heating in Huber CC 304 heater) holding at 200°C for low-temperature aging. The heating rate is measured to be 50°C/s by attaching a thermocouple to the sample. *In-situ* tensile Electron BackScatter Diffraction (EBSD) method is reported in our recent paper [10]. The primary deformation mechanisms in more than 1000 grains randomly selected at yielding was characterized by in-situ tensile EBSD. A JEOL 2100plus transmission electron microscope (TEM) operating at 200kV is used to characterize microstructural details beyond EBSD resolution. *In-situ* tractions in TEM are conducted by using a Gatan heating-straining holder. The observations are recorded as short videos with Gatan Rio 16 CMOS camera. Samples for ex-situ TEM observations are cut from the deformed samples after in-situ EBSD tests. All the samples for TEM observations are thinned by twin-jet electropolishing, using a solution of 4% perchloric acid in methanol at -15 °C. The Schmid factor (SF) is defined as: SF = $\cos\lambda \cos\varphi$, where λ and φ are the angles between the tensile direction and the normal to habit plane (or the twinning plane) and the associate invariant strain direction (or the twinning direction), respectively. The values of λ and φ in each grain are accessed by the EBSD data. In addition, nanometer-scale compositional analysis of the same samples was done using a CAMECA LEAP 5000XS 3D atom probe microscope operated at 30 K with a pulse fraction of 20% and a detection rate of 0.5 in Laser mode.

3. Results

3.1 Tensile properties of ω_{iso} strengthened Ti-12Mo

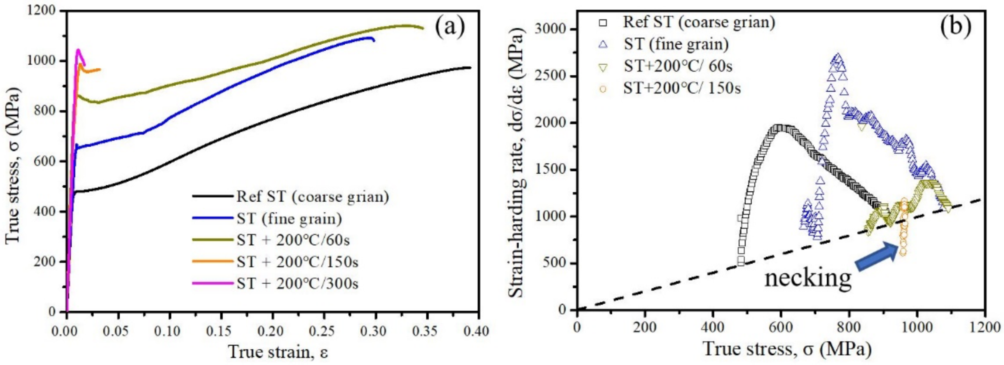

Figure. 1 (a)The true strain-stress curves of the Ti-12Mo at different states. (b) The corresponding strain-hardening rate curves of Ti-12Mo sample as a function of true stress.

Figure 1 shows the true strain - true stress curves of Ti-12Mo alloys at different states. At solution-treated (ST) state, two tensile curves are shown of classic coarse-grain (average grain size = 100±5 μm) studied in previous works [1, 9] and the fine-grain (average grain size = 20±2 μm) used in this study. It can be seen that the yield and flow stresses of the ST (fine grain) are both enhanced when compared to the ST(coarse grain) alloy, whereas the uniform elongation decreases to about 0.3. The strengthening treatments are thus performed on the ST (fine grain) samples in order to trigger TRIP and TWIP mechanisms at high yield stress. The ω_{iso} strengthen temperature is fixed at 200˚C in the ω_{iso} precipitation range between the 150˚C and 475˚C [9, 18]. Different aging durations, 60s (ST+200˚C/60s), 150s (ST+200˚C/150s), and 300s (ST+200˚C /300s), are selected in the early stage of the precipitation according to a previous thermodynamic analysis by electrical resistance measurements [18].

After aging at 200˚C for 60s (ST+200˚C/60s), the yield stress increases from 659MPa to 865MPa on the ST (fine grain) alloy, while the uniform elongation increases from 0.3 to 0.35, close to that of the ST(coarse grain) alloy. After increasing the durations of heat-treatment at 200˚C, the uniform elongation dramatically decreases to

0.033 after 150s (ST+200°C/150s) and is observed to be completely inhibited after 300s (ST+200°C/300s) as shown in figure 1a. For the ST+200°C/150s sample, the yield stress reaches about 1GPa during the tensile test without embrittlement (still ductile fracture) but severe necking. The hardening rate decreases rapidly since the yield point, then the necking happens when it drops below the Considère criterion line (the dashed line: $d\sigma/d\varepsilon = \sigma$ in Figure 1b) at $\varepsilon = 0.03$. The uniform elongation is thus very limited when compared to the ST(fine grain) samples and ST+200°C/60s sample. After further aging to 300s (ST+200°C/300s), the sample exhibits high strength (1048 MPa) but almost no ductility (brittle Fracture). The elastic moduli (table s1 and Figure 1a) of the samples increase from 80 GPa (ST) to 110 GPa (ST+200°C 60s and ST+200°C/150s) then 140 GPa (ST+200°C/300s). The strain-hardening rate ($d\sigma/d\varepsilon$) curves of the samples are shown in Figure 1b. The curves of the ST(fine grain) and ST(coarse grain) are non-monotonic, similar to those often observed in TRIP/TWIP β Ti-alloys [1,2,18-27], their hardening rates reach respectively the maximum values, of 1975MPa and 2685MPa, at $\varepsilon = 0.1$. After 60s aging, an important reduction of the strain-hardening rate can be noticed, but the rate is still high enough (above the Considère criterion line in Figure 1b) to maintain the uniform elongation till $\varepsilon = 0.35$.

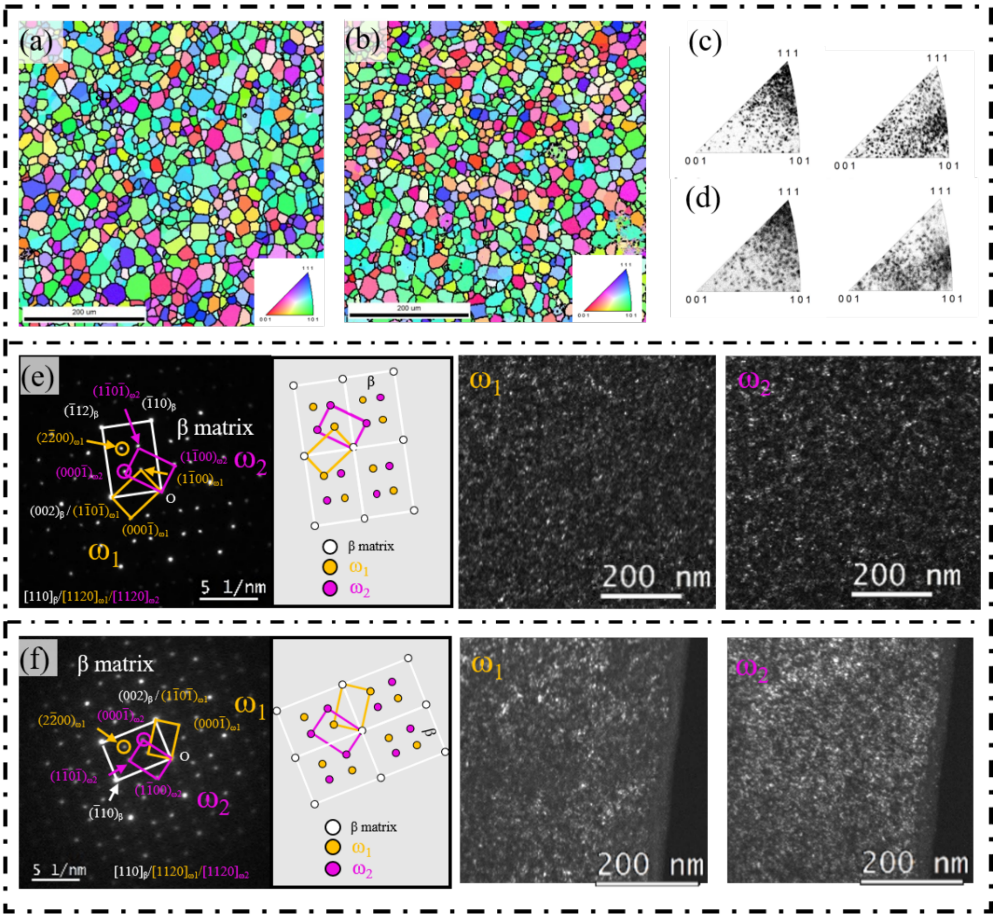

Figure 2 Initial microstructure of ST (fine grain) and ST+200°C /60s sample: Inverse pole figure maps of (a) ST (fine grain) and (b) ST+200°C /60s samples; inverse pole figure of the grain orientations at ND and RD directions of (c) ST (fine grain) and (d) ST+200°C /60s samples; electron diffraction patterns from (e) ST (fine grain) and (f) ST+200°C /60s samples and the corresponding dark-field TEM images of ω precipitates; ND: normal direction, RD: rolling direction.

Figure 2 presents the fully recrystallized grain structures of the ST (Figure 2a) and ST+200°C /60s (Figure 2b). The equiaxial β grains are of 20 μm in average size in both states. No change can be seen on the grain size or orientation distribution in ST (Figure 2c) and ST+200°C/60s (Figure 2d). Dark field TEM micrographs along $[110]_\beta$ zone axis are shown in Figure 2e (ST) and Figure 2f (ST+200°C/60s), where no observable difference on ω diffraction or precipitate size can be identified.

3.2 ω phase transformation characterized by in-situ heating in TEM and atom probe tomography

An *in-situ* heating TEM observation is performed to follow the changes of ω phase during the heating process to 200°C. Figure 3a shows the TEM micrographs of the selected zone in a β grain tilted to $[110]_\beta$ zone axis in ST (fine grain) sample before heating. The $[110]_\beta$ zone axis diffraction pattern shows sharp reflections at the 1/3 and 2/3 $\{112\}_\beta$ locations, indicative of a well-developed fully-collapsed (of $\{111\}_\beta$ planes) structure within the ω precipitates. This is consistent with previous observations [28,29]. A dark-field image recorded using the reflections from one of the ω variants is shown in the same figure. Upon heating, the selected zone is kept in view by shifting the sample against the drift caused by thermal expansion. The zone axis is maintained at $\{110\}_\beta$ by fine-tilting. It is noticed that the ω reflections are steady during the entire heating process without visible change. Figure 3b presents the bright/dark field images and the corresponding diffraction pattern recorded in case of the sample heated to 200°C for 60s. Again, the sharp reflections at the 1/3 and 2/3 $\{112\}_\beta$ locations are indicative of a well-developed fully-collapsed (of $\{111\}_\beta$ planes) structure within the ω precipitates. Additionally, the density, size (3-5 nm) and morphology of these ω precipitates do not show significant difference when compared to the images taken before heating (Figure 3a).

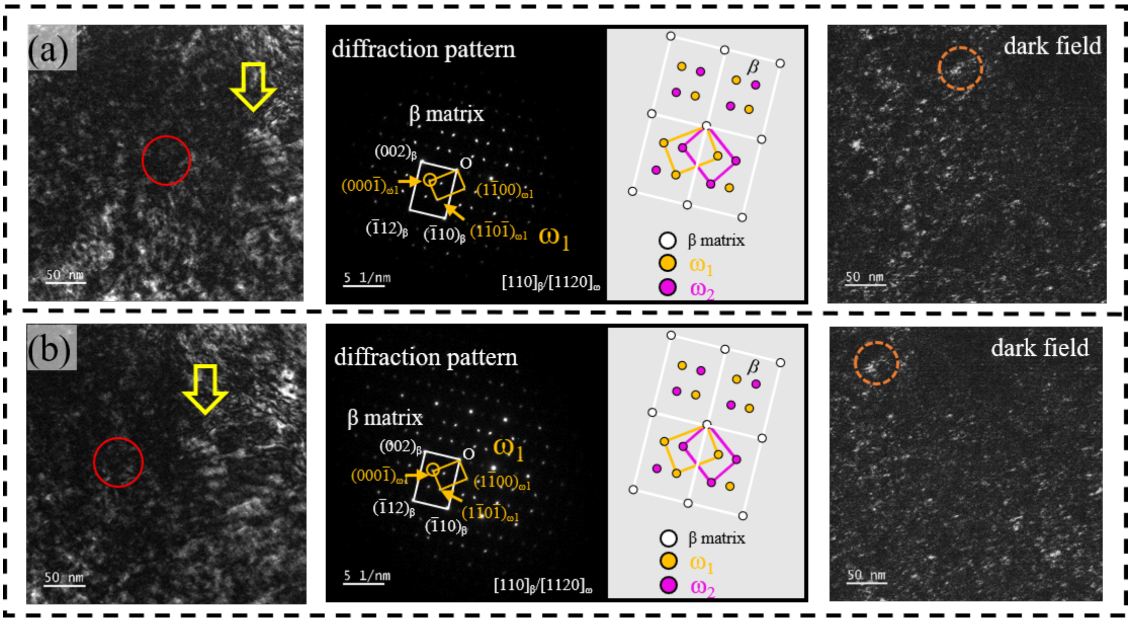

Figure 3 In-situ heating TEM investigations: (a) before heating, (b) after heating at 200°C for 60s (observed at 200°C).

In order to investigate the ω_{iso} phase, chemical micro-analysis by atom probe tomography is employed on the samples ST + 200°C/60s and ST + 200°C/150s. Fig. 4(a-b) and 4(c-d) shows the APT analysis of ST + 200°C/60s and ST + 200°C/150s respectively. The Ti raw ion map in Fig. 4(a) shows no obvious partitioning. However, the homogeneity of Ti ions has further been investigated using radial distribution function (RDF) [30]. The RDF in Fig. 4(b) shows that for a Ti center atom, the concentration of Ti is higher than bulk within a radius of 2 nm, indicating Ti-rich clusters of ~2 nm radius. Based on the evidence of Ti clustering in RDF, cluster analysis algorithm [31,32] was used to reveal the quantitative details of Ti-rich clusters. The inset in Fig. 4(b) shows the spatial distribution of Ti-rich clusters within a 30×30×40 nm^3 volume of the APT reconstruction. As tabulated in Fig. 4(e), these Ti-rich clusters which are potential ω_{iso} particles were found to contain ~96.4 at.% Ti and 3.6 at.% Mo on average as compared to ~93.6 at.% Ti and 6.4 at.% Mo in the bulk. Further, the volume fraction and average radius of these clusters were found to be 4% and 1.26 nm respectively, based on the cluster analysis algorithm employed. The slight discrepancy in the radius of clusters between RDF and cluster analysis is due to their algorithms and the actual radius of cluster could be somewhere between 1.26 and 2 nm. Similarly, Fig. 4(c) shows a homogenous distribution of Ti in the APT raw ion map obtained from ST + 200°C/150s condition. However, RDF in Fig. 4(d) reveals Ti enrichment up to a radius of ~2.5 nm around Ti atoms. The Ti-rich clusters from cluster analysis are shown in the inset of Fig. 4(d). These clusters were found to be marginally enriched in Ti but with increased volume fraction. The cluster radius was found be on the same scale as ST + 200°C/60s condition. The comparison of APT analysis from the two aged conditions reveals that more ω_{iso} particles have nucleated with increase in aging time along with a marginal increase in Ti concentration. The Mo concentration in clusters of both conditions is lower than that of quenched-in ω_{ath} precipitates (≈6.37 at.% or 12 wt. %) which inherit the composition of the parent β matrix in the same Ti-12Mo alloy [9, 29], suggesting that these clusters/domains could probably be the ω_{iso} precipitates at the early stage of Mo-depletion process, which can finally reach 1.8 at.% Mo after ω_{iso} growth for 48h at 475°C [29]. This indicates that the rejection of Mo from the ω_{ath} precipitates during isothermal aging, potentially leads to the formation of the ω_{iso} precipitates. Furthermore, the reduction of Mo concentration in ω_{iso} nuclei can increase remarkably the elastic moduli [19] as well as energy barriers to slip activation [16] in ω lattice. The experimentally determined Youngs moduli of the ST + 200°C/60s and ST + 200°C/150s samples are 110~120 GPa, which are substantially higher than that observed in case of the ST state (~80 GPa). These results also agree to the systematic studies conducted in Ti-15Mo (wt.%) on elastic constants variation during temperature cycling [20], where the constants recorded in ST (fine grain) state are lower than those in the samples after aging to 300°C.

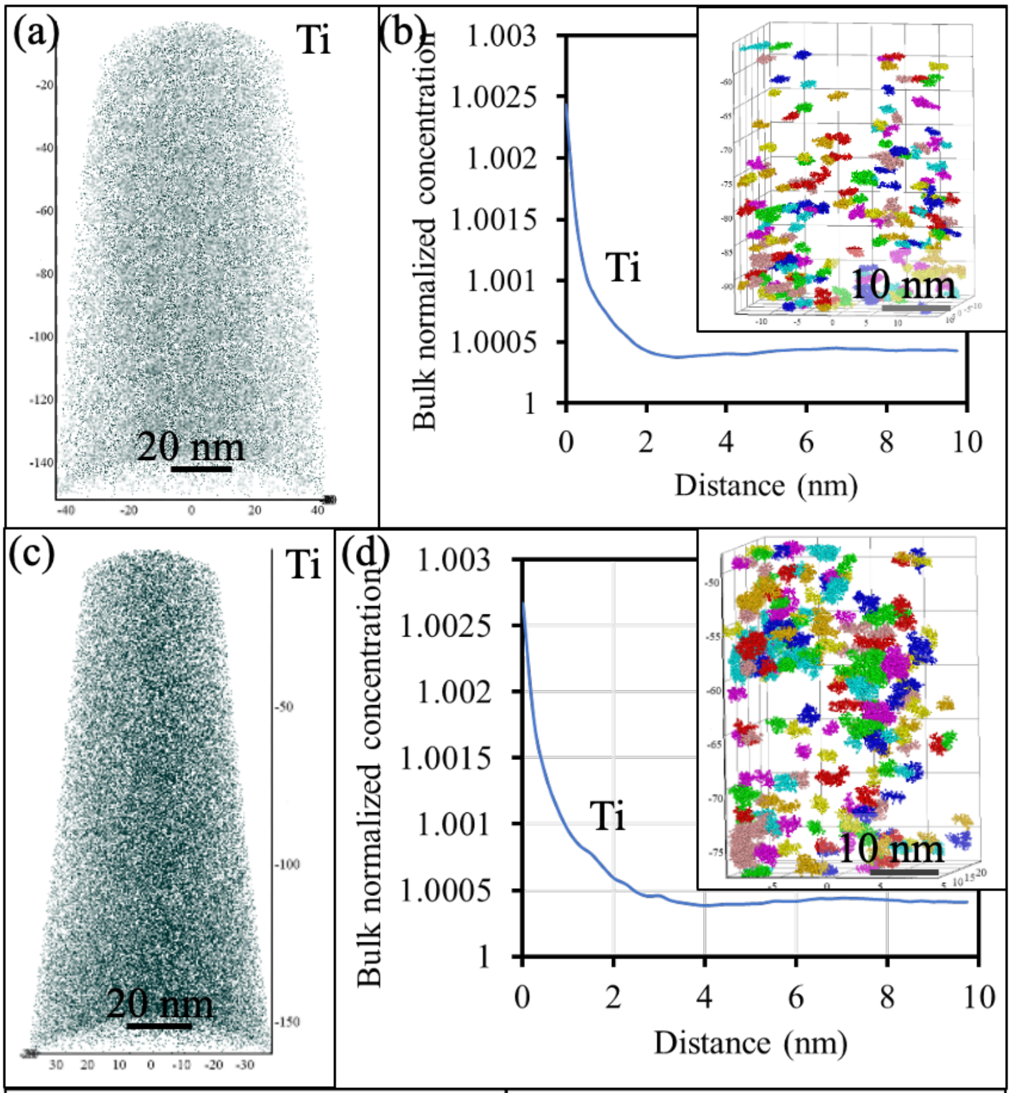

(e) Cluster anlaysis		Cluster anlaysis	
Ion	Ti	Ion	Ti
Volume fraction	4	Volume fraction	8
Average radius (nm)	1.26	Average radius (nm)	1.14
Mo at.%	3.62	Mo at.%	3.31

Figure 4 Atom probe tomography (APT) results from (a-b) the ST + 200°C/60s sample and (c-d) the ST + 200°C/150s sample: (a and c) raw ion map of Ti and (b and d) radial distribution function maps of Ti ions; (e) cluster analysis from the ST + 200°C/60s sample and the ST + 200°C/150s sample.

3.3 Deformation mechanisms investigated by in-situ EBSD and TEM observations

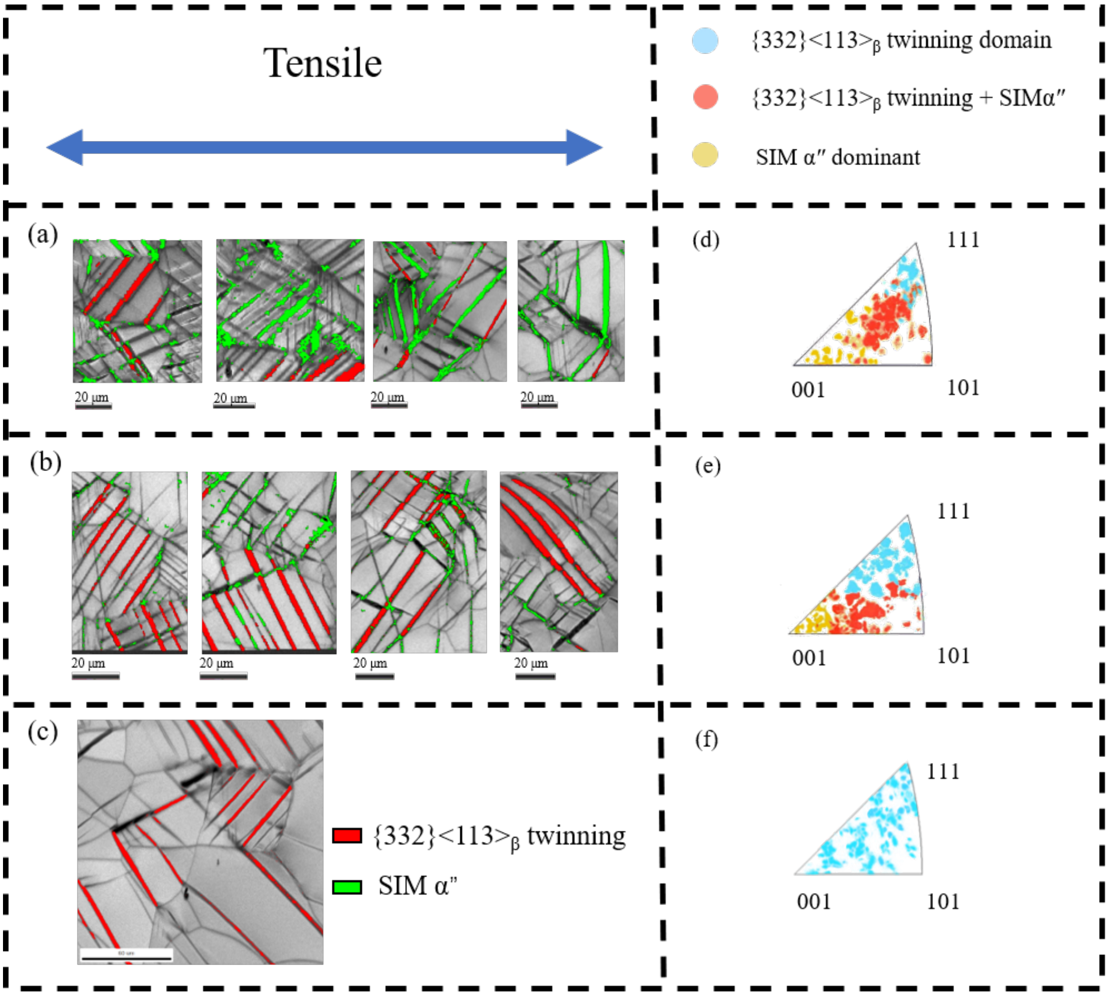

Figure 5 Experimental EBSD statistic of the primary deformation products in different grains in ST (fine grain), ST + 200°C/60s, and ST + 200°C/150s samples by in-situ EBSD under tensile strain (ε =0.02): several cases of IQ maps of ST (fine grain) (a), ST + 200°C/60s (b), and ST + 200°C/150s (c) alloys; Experimental Inverse pole figure (IPF) of the statistic of the primary deformation products in ST (fine grain) (d), ST + 200°C/60s (e), and ST + 200°C/150s (f) alloys.

The *in-situ* EBSD is carried out to trace the deformation mechanisms, mechanical twinning, and reversible β → α″ martensitic transformation, of the ST (fine grain), ST

+ 200°C/60s, and ST + 200°C/150s. In each sample, about 1000 grains randomly selected are analyzed by in-situ tensile test coupled with EBSD mapping in these three microstructural states. The band-like deformation-induced products, i.e., 332T and SIM α″, are identified in each grain at yielding point (ε=0.02) for statistics. Example EBSD maps in each sample are shown in Figure 5 (a-c), in which either SIMα″ or 332T or both mechanisms are observed in different grains depending on the grain orientation. Figure 5 (d-f) shows the EBSD statistical analysis of the transformation products in these grains. The statistics in inversed pole figure demonstrate the partition of the deformation mechanisms as a function of grain orientation, which is called transformation partition mapping (TPM) [10]. The TPM approach reveals the orientation dependence on deformation mechanism selection. The TPM method is mostly useful at the onset of the plastic regime where the stress distribution is mainly determined by the initial microstructure and the elastic anisotropy of the polycrystalline aggregate, compared to further states when the deformation in neighboring grains might influence the selection of deformation mechanisms. Thus, this method can be applied to compare quantitatively the TRIP and TWIP mechanisms in the alloys in case of similar starting phases and microstructures. The interpretation of the experimental TPM is associated to the theoretically calculated TPM by combining different Schmid factor (SF) thresholds of each mechanism. The SF threshold of a mechanism measures statistically the lower bound of SF above which the mechanism can be activated at yield point under uniaxial tensile loading. Figure 6 presents 9 calculated TPMs in the SF threshold range of 0.3-0.38 for α″ and 0.35-0.45 for 332T, where the one in the center (marked by red dash square) corresponds the best to the experimental TPM of coarse grain Ti-12Mo [10].

The cases framed by blue color and purple color in Figure 6 present the best agreement of transformation partition maps between calculation and experiment of ST (fine grain) and ST + 200°C/60s, respectively, suggesting that the Schmid factor threshold of SIM α″ equals to 0.3 and of 332T equals to 0.4 in ST (fine grain); the Schmid factor threshold of SIM α″ equals to 0.38 and of 332T equals to 0.35 in ST + 200°C/60s alloy. Besides, the Schmid factor threshold is about 0.3 for 332T in the ST + 200°C/150s, whereas the SF threshold is no longer valid for SIM α″ since it is completely suppressed.

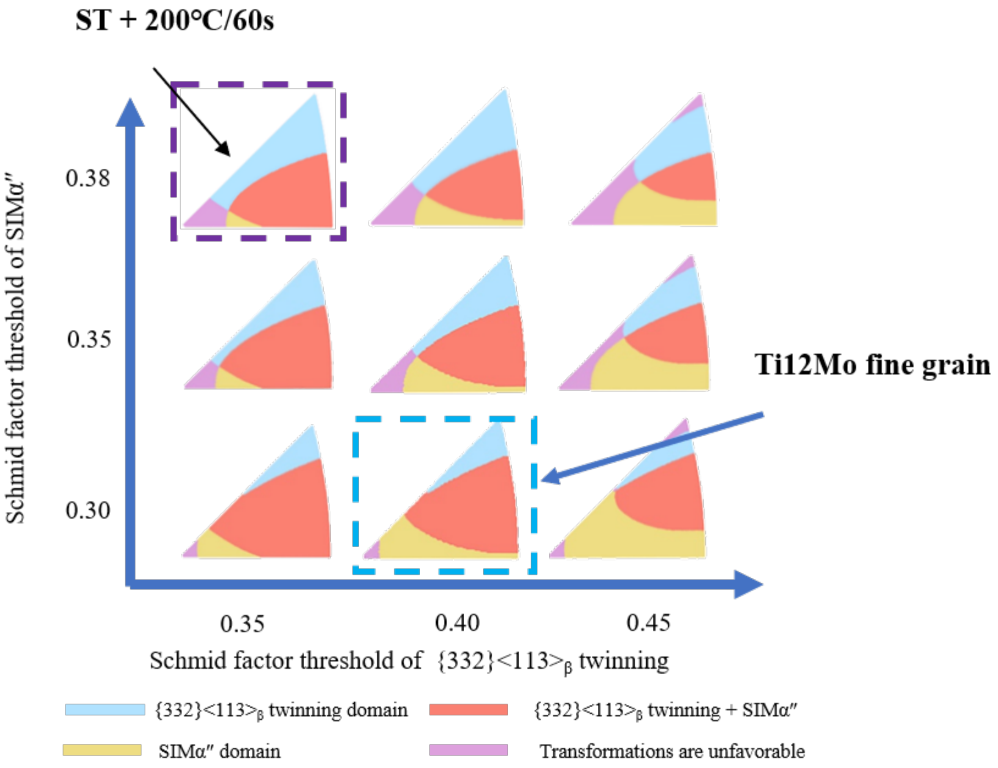

Figure 6 Inverse pole figures of the calculation of the orientation domains as a function of the combinations of threshold Schmid factors. The cases marked by dash square confirm the domain distribution observed experimentally in ST (fine grain, blue) and ST + 200°C/60s (purple) alloys.

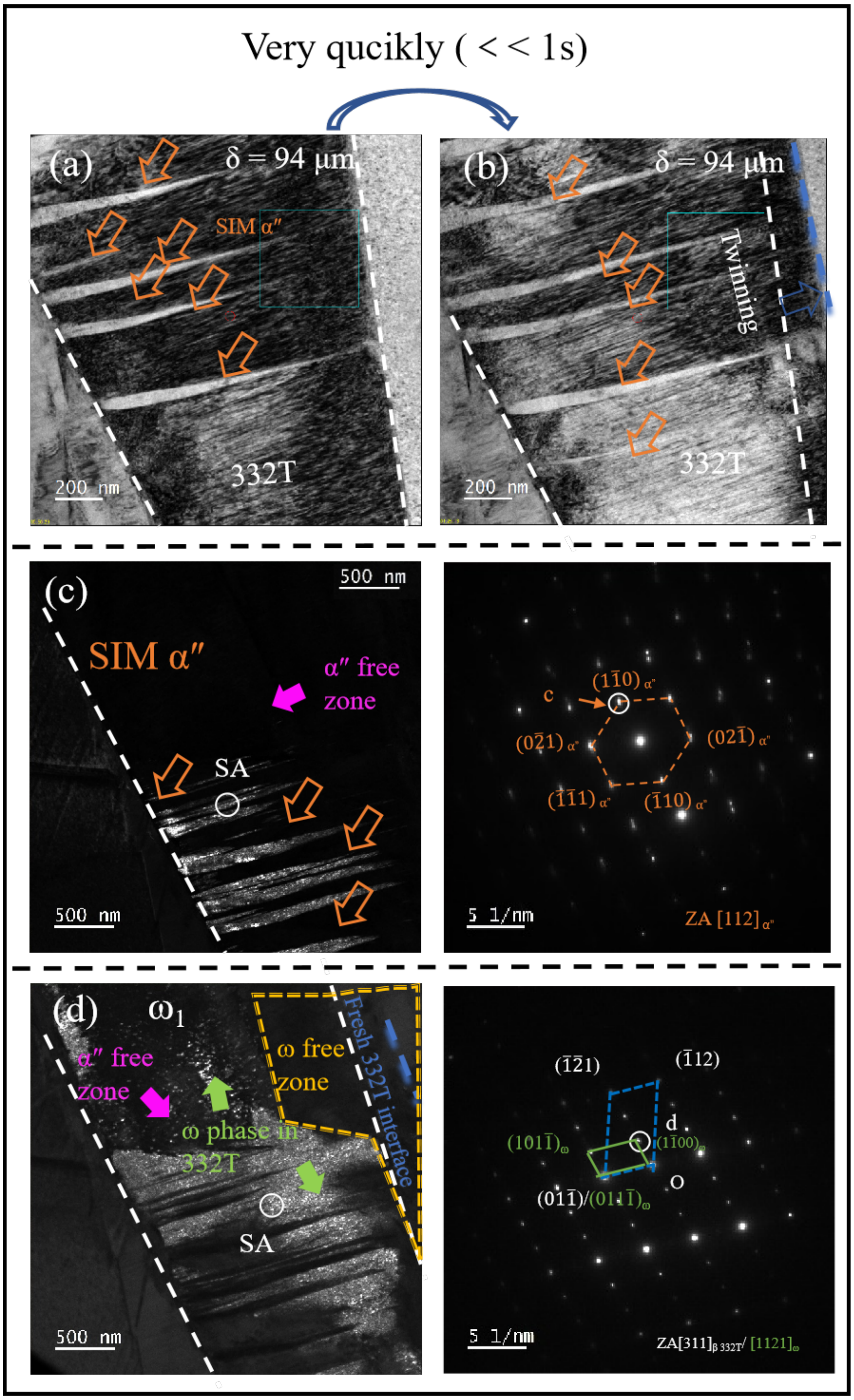

Figure 7 In-situ tensile TEM investigations of 332T at ST + 200°C/60s sample after deformation: (a-b) bright field image; (c-d) SAED pattern taken from the region indicated by white circles and corresponding dark-field images of one variant of SIMα″and of the ω phase, respectively.

To investigate the interaction between ω phase and 332T during the thickening of the twin band, careful in-situ tensile TEM investigations are performed (Figure 7) on a ST + 200°C/60s sample at undeformed state. During increasing the tensile strain on the TEM sample, a band-like deformation product with width of 900 nm forms and is identified as a 332T. In the twin band, 2nd SIM α″ bands are identified by diffraction analysis and imaged in corresponding dark-field image (Figure 7c marked by orange arrows). These 2nd SIM α″ bands continue to grow until they reached the boundary of the 332T band (Figure 7a and b, and video in supplementary material). The coarsening process of the 332T is acute during the straining. The expansion of the 332T boundary from white dash line marked in Figure 7b to the blue dash line is very rapid, much less than 1s, then stops (Figure 7a and b, and video in supplementary material). Such behavior is very different than the kinetic of martensite coarsening in the same sample, which is observed in a continuous manner with a nearly constant rate of interface movement [33]. The TEM sample is then tilted to [011] zone axis of the twinning bands without releasing the tensile load. The dark-field imaging of ω in the twin band demonstrates a heterogeneous distribution of the ω phase (Figure 7d), unlike the homogenous distribution of ω phases in the undeformed β matrix (Figure 2 e and f). It should be noticed that a zone near the fresh 332T interface (marked by blue dashed lines in Figure 7) is free of ω phase (marked by yellow color). The ω phase is found in the rest volume of 332T as shown in the dark field image of ω phase in Figure 7d. After checking different zones in the 332T, it is found that all the ω phase is of the single variant as shown in the diffraction pattern (insert in Figure 7d). Most of these ω precipitates distribute in the vicinity of secondary α″ bands. The thickening process of

332T is observed to be a rapid transformation of a volume of β matrix to 332T without the observations of ω lamellae or α″ at the twin boundary, as sometimes reported [3,33].

The dislocation activities are examined in ST + 200°C/60s and ST + 200°C/150s samples after deformation (Figure 8). The burgers vectors of the dislocation lines is analyzed by using the three ***g.b*** = 0 extinction conditions around [111]β zone axis (Fig. 8). It can be seen a set of dislocation lines is composed by a group of screw dislocations attributed to three Burgers vectors b=a/2<111> (labeled by b1, b2 and b3 in the Fig. 8). As shown in Figure 8a, the β matrix is divided into rectangular sub-domains by the twin network, and a high density of dislocations with three Burgers vectors b=a/2<111> can be observed concentrated around the twin boundary. In the contrast, only a few individual dislocations (marked by blue arrows in Figure 8b) with burgers vector b_1 could be observed in the isolated β matrix under g_2 and g_3 conditions (Figure 8b). It can be noticed that, when comparing to 60s sample (dislocations marked by blue arrows in Figure 8b), the density of the dislocations is less important in the ST + 200°C/150s sample and only one dislocation glide system (b_1) is observed. The low dislocation density indicates that the dislocation glide is strongly suppressed in the ST + 200°C/150s alloy (Figure 8a).

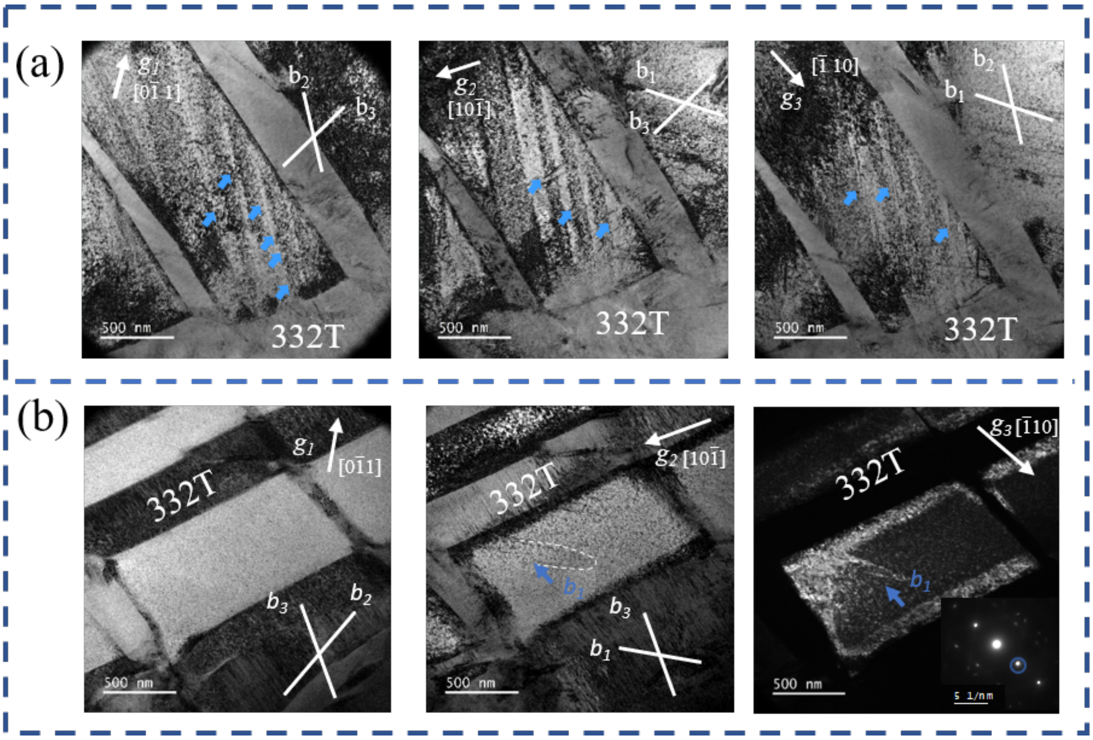

Figure 8 (a) ex-situ TEM micrographs of ST + 200°C/60s alloy at ε=0.02: bright field images of $g_1 = [0\bar{1}1]$and $g_2 = [10\bar{1}]$, and dark field images of $g_3 = [\bar{1}10]$ conditions around [111] $_\beta$ zone axis; (b) ex-situ TEM micrographs of ST + 200°C/60s alloy at ε=0.02: bright-field images of $g_1 = [0\bar{1}1]$, $g_2 = [10\bar{1}]$, and $g_3 = [\bar{1}10]$ conditions around [111] $_\beta$ zone axis.

4. Discussion

4.1 Formation of ω_{iso} precipitates

The transformation from ω_{ath} to ω_{iso} is a diffusion-controlled process involving Mo rejection, possibly initiating from pre-existing sites as indicated by isothermal thermodynamic analysis [21-23]. The microstructure after low-temperature aging for short durations is a β matrix with well-dispersed ω_{iso} precipitates at the early stages of formation. The sizes and distribution of ω precipitates before and after aging do not show significant change under TEM observations by dark-field imaging (Figure 2e and 2f). The diffraction patterns obtained from both ex-situ (Figure 2e and 2f) and in-situ

(Figure 3a and 3b) observations before and after the aging treatments are nearly identical, indicating that the presence of the ω phase, the variants of ω precipitates, and their orientation relationships with β matrix are not affected by the isothermal aging at 200°C. The possible change induced by the short aging could thus be on the aspect of chemical composition. Devaraj et al. [11] have shown that the formation of the ω_{ath} precipitates during water-quenching results in the Mo atoms trapped within these precipitates in a metastable "frozen" state [34] The thermal activation, i.e. aging at ω_{iso} precipitation temperature range, provides the necessary driving force to "unfreeze" the Mo atoms by diffusion out of the ω_{ath} precipitate. The Mo depletion leads to chemical stabilization of the ω crystal structure towards perfect collapse degree (hexagonal lattice) and eventually the growth of ω_{iso} particle showing diffusion-controlled kinetics [18] The depletion of Mo in ω_{iso} also significantly increases the shear modulus of the ω phase which is responsible for the significant strengthening effect observed in β Ti alloys which has been isothermally aged to promote the formation of ω_{iso} precipitates [11,13,14,29]. In this study, the APT results reveal that the rejection of Mo is detected as nanometer-size Ti-rich clusters in which Mo concentration is lower than that in the surrounding β matrix (Figure 4). The size of these Ti-rich / Mo-lean clusters is at the same order of magnitude as that of the ω_{ath} precipitates. These results indicate that these clusters are the early stages of formation of ω_{iso} precipitates, during the aging at 200°C for short durations. The coarsening of the ω_{iso} phase has probably not begun due to the limited Mo-diffusion rate at such temperature near the lower bound of the ω precipitation range [9,11,13].

4.2 CRSS changes of mechanical twinning and SIM α″ due to isothermal ω precipitation

It can be seen from the above results that the formation of ω_{iso} nanoprecipitates increases considerably the yielding stress of the samples, as well as the Young's moduli. Figure 9 summarizes these mechanical properties as a function of thermomechanical treatment histories. The strengthening effect due to ω precipitation has been comprehensively studied in many researches [14,24,25].

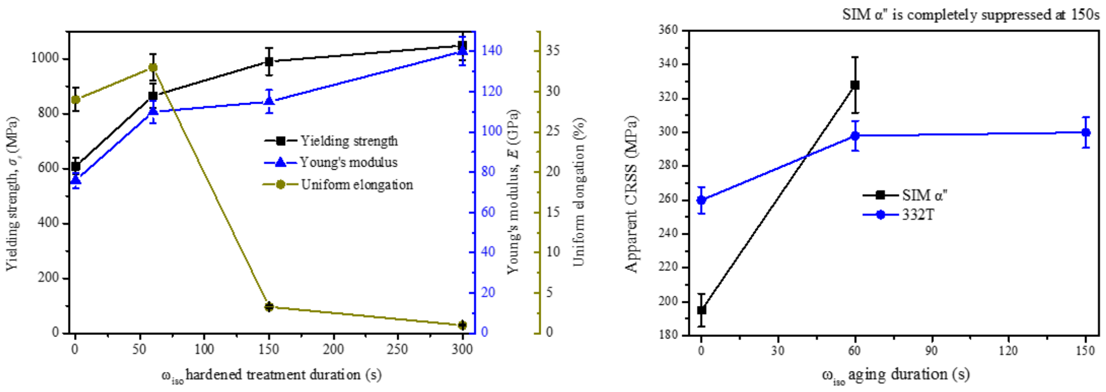

Figure 9 (a) the yielding stress, Young's modulus, and uniform elongation of Ti-12Mo alloys as a function of, (b) the apparent CRSS of 332T and SIMα″ as a function of ω_{iso} aging treatment duration.

According to the TPM analysis, the distributions of deformation products (SIMα″ and 332T) of the experimental transformation partition maps show significant differences depending on the thermal treatment history. Taking the TPM of ST (fine-grain) as a reference, the orientation domains in blue and red (Figure 5c) locates the grains that can choose 332T as a deformation mechanism to respond to the local stress. Similarly, the grains in domains red and yellow are those in which the SIM α″ is a possible candidate as operational mechanism. In ST + 200°C/60s sample, the grain orientations favorable for 332T (blue + red domains) are not significantly changed, compared to ST (fine grains), whereas the orientations favorable for SIM α″ (yellow + red domains) occupy much less area than that of fine-grain Ti-12Mo. The phenomenon is characterized by the increase of the SF threshold of SIM α″ mechanism from 0.3 in fine-grain 12Mo to 0.38 in 60s aging 12Mo. The increase of SF threshold indicates that less grain orientations, in fact, less grains since the samples have the same size and texture, are favorable for SIM α″ mechanism. The same trend continues in the ST + 200°C/150s sample, in which SIM α″ is completely suppressed without any α″ phase observed during the in-situ EBSD statistic. The absence of SIM α″ suggests that the critical resolved shear stress (CRSS) of such phase becomes higher than the maximal shear stress that can be induced at yield point. Since the SF threshold and CRSS interrelate, it is of interest to discuss the relationship between them for each deformation mechanism.

According to Schmid law [36], a deformation mechanism can be operational in one grain in the assembly polycrystalline when satisfying:

$$\sigma_{grain} \cos\psi \cos\lambda \geq \tau_{critical} \qquad eq.2$$

where the σ_{grain} is the local stress undertaken by the grain, $\cos\psi \cos\lambda$ is the Schmid factor of a given set of lattice plane and shear direction in the grain, $\tau_{critical}$ is the CRSS of the deformation mechanism operating along the above plane and direction. The SF threshold measured by in-situ EBSD is the statistical minimum of the SF that satisfies Eq.2 in the assembly of the grains. Therefore, the apparent CRSS ($\tau_{critical}$) of each deformation mechanism in a polycrystalline assembly at yield point can be estimated by the following equation:

$$apparent\ \tau_{critical} = \sigma_{yield} SF_{threshold} \qquad \text{eq.3}$$

where σ_{yield} is the yield stress of the grain assembly under uniaxial tensile loading. To estimate the apparent CRSS is an approximative approach usually used in the studies involving multiple slip systems in polycrystalline alloys, sometimes with multiple phases, where the precise determination of σ_{grain} is usually difficult. The absolute values of apparent CRSS determined by Eq. 3 are indicative, allowing comparative evaluations between deformation mechanisms in the samples with similar phase constitution, grain size, elastic anisotropy and texture under the same deformation conditions. In this study, the ST (fine grain) alloys with different aging states are of the same morphologic and crystallographic textures as well as comparable phase constitutions and elastic anisotropy. By comparing the apparent CRSS among different mechanisms under different aging conditions, the tendency of how mechanisms evolve as a function of aging duration can be visible in Figure 9b. After ω_{iso} aging for 60s (ST + 200°C/60s), both the apparent CRSS of SIM α″ and 332T increased (Figure 9), which suggested that both the TRIP and TWIP effect requires higher local shear stresses for activation when comparing to ST (fine grain) alloy. After ST + 200°C/150s, the apparent CRSS of 332T increases slightly and the SIM α″ is completely inhibited (Figure 9). It is suggested that the increases of CRSS of both mechanisms are due to the increasing sites where ω_{iso} nucleated, as this is the only varying parameter.

4.3 Deformation mechanism shift as a function of isothermal ω aging

For SIM α″, the Mo enrichment in the vicinity of the ω nuclei can stabilize the β phase then increase the energy barrier for nucleation and growth of α″ martensite. The stability of β matrix increases due to the locally concentrated Mo elements (as shown in figure S1), thereby suppressing chemically the formation of SIM α″. Moreover, Kim et al. [26] suggested that the SIM α″ transformation from β matrix is mediated by the shuffling of $\{110\}_\beta$ planes with <110> directions. Lai et al. [15] implied that ω phase is a strong obstacle to the collective $\{110\}<110>_\beta$ atomic movements involved in the martensitic transformation. They also implied that the degree of the obstacle effect in ω phase is related to the shear modulus on the $\{1120\}_\omega$, which is parallel to $\{110\}_\beta$ according to the orientation relationship between ω and β. Sallom et al. [19] reported that the shear modulus of ω_{iso} is larger than that of ω_{ath}. The computation in [19] demonstrates that the c44 increases from about 45 GPa to 55 GPa when Mo concentration in ω phase decreases from 12 wt.% (6.37 at.%) to 7 wt.% (3.62 at.%), which is the concentration of the Mo-lean cluster after 60s aging (Figure 4a). The larger shear modulus of ω_{iso} thus obstructs the $\{110\}<110>_\beta$ shuffle movement, which limits the α″ martensitic transformation. Therefore, the ω_{iso} precipitation results in a stronger hindrance to the martensitic transformation resulting in an increase of apparent CRSS of SIM α″. The sum of both effects stated above is responsible to the increase of the apparent CRSS of SIM α″, from 195 MPa to 330 MPa, after aging for 60s. And finally, the TRIP effect is fully suppressed after aging for 150s, which suggests that the apparent CRSS should be superior to 500 MPa, which is the maximal apparent shear stress at yield point in the grains with SF = 0.5.

On the other hand, 332T shows quite a tolerance to the increment of the ω aging durations. The apparent CRSS of 332T increases from 260MPa (ST state) to 290 MPa (ST + 200°C/60s) then to 300 MPa (ST + 200°C/150s). Complete suppression of 332T is observed in ST + 200°C/300s sample. As observed in the in-situ TEM experiment under traction, the destruction of ω precipitates happens during 332T processes, resulting in an ω-free zone in the freshly twinned region (Figure 6d). The result confirms the assumptions discussed in previous ex-situ studies [17]. The different tolerance to ω aging may be due to the different transition pathways between 332T and SIM α″ at atomic level. It has been reported that the 332T product can be obtained via the reversion from twinned α″ martensite precursor [37] However, this pathway is no longer available when the α″ transformation is fully supressed, as seen in ST + 200°C/150s. An alternative pathway has been suggested by ab-initio calculation that the 332 twinning operation can be dissociated to a $(21\bar{1})$ $[\bar{3}\bar{1}1]$ shear plus shuffles on (011) plane along $[2\bar{3}3]$ and $[\bar{2}3\bar{3}]$ directions [335] Along this pathway, α″ precuseur is not mandatory in the formation of 332T, thus the 332T mechanism can be still operational in ST + 200°C/60s and ST + 200°C/150s aging samples in which β → α″ transformation has been completely inhibited. In agreement with ab-initio calculation, the experimental observation here implies again that the atomic-level mechanism of the 332T origin can be very different than that of the β → α″ → twinned α″ → 332T sequence in Ti-12Mo.

The dislocation slip is the third deformation mechanism operational in the ST [10] and 60s aging samples (Figure 8). The formation of a twins and martensite needles network refines the dislocation mean free path and contributes to the strain-hardening effect. However, the EBSD-based TPM method cannot detect the slip system activation. Therefore, its apparent CRSS is unknown and cannot be compared with the other mechanisms under different ω_{iso} states. The first principal studies [19] have investigated comprehensively the slip energy barriers of slip systems in the β and ω phases. And the energy barriers increase with the depletion of Mo in ω phase [19]. By comparing the ST + 200°C/60s sample and ST + 200°C/150s sample after deformation, the dislocation operations are found much less active in the ST + 200°C/150s sample (Figure 9). Nevertheless, the 332T network in both samples is quite similar. It is therefore thought that the 332T is the dominant deformation mechanism to accommodate the plastic strain in the ST + 200°C/150s sample. Without massive dislocation slip, the dynamic Hall-Petch effect breaks down, leading to the low strain-hardening rate and therefore rapid necking by strain localization observed in ST + 200°C/150s sample. The formation of 332T network without dislocation slip can contribute around 0.033 elongation without hardening effect. To sum up, the deformation mechanism in Ti-12Mo alloys can be shifted as a function of aging time at 200°C as shown in table 1.

Table 1 Major deformation mechanisms observed in Ti-12Mo alloys after different heat treatments from as-cold-rolled state.

	ST (fine grain)	ST + 200°C/60s	ST + 200°C/150s

TRIP	Favorable	Active	Not observed
TWIP	Active	Favorable	Favorable
Dislocation slip	Active	Active	Unfavorable

The results indicate that the formation of ω_{iso} precipitates leads to the strong suppression of all three mechanisms: SIM α'', 332T and dislocation slip. However, the tolerance of each mechanism to the ω_{iso} formation is different. SIM α'' is the most sensitive mechanism to ω_{iso} formation when compared to the 332T and dislocation slip. Between 332T and dislocation slip, it is unexpected that the dislocation activities are strongly perturbated in the ST + 200°C/150s aging sample while 332T is well operational. Thus, the suppression of deformation mechanisms induced by ω_{iso} formation is different than that induced by changing chemical stability of β phase. When β stability is increased by adding β stabilizers, the dominant deformation mechanism shifts from a combination of SIM α'' + slip, to SIM α'' + mechanical twinning + slip, to mechanical twinning + slip, and then to single slip mechanism, [4], in Ti-Mo and other systems [15-17]. Along with the increase of β stability, the alloys are gradually deprived of TRIP and TWIP effects because the CRSSs of SIM α'' and 332T increase strongly, and overpass that of dislocation slip. In order to keep TRIP and TWIP effects at high yield stress, the CRSS of dislocation slip must be increased correspondingly with the other mechanisms in a way that the chemical stability of the β phase stays in the composition range favorable for SIM α'' and 332T. The ST + 200°C/60s sample in this study showcases that ω_{iso} formation is a practical solution to achieve TRIP and TWIP effects at 859MPa yield stress. Moreover, the ST + 200°C/150s sample proves that 332T can still be operational at yield stress close to 1 GPa yield stress in a simple binary Ti alloy. The further development of high strength TWIP Ti alloys via ω_{iso} strengthening is a promising new development path.

5. Conclusions

(1) The ω_{iso} strengthening effect offers an applicable hardening strategy for TRIP/TWIP Ti-12Mo alloy to achieve greater yield and flow tensile strength with large ductility. The ST + 200°C/60s alloy can deliver the best balance between yield strength and ductility. The drop of the hardening rate at ST + 200°C/150s sample could probably be due to the suppression of dislocation glide by ω_{iso} precipitates.

(2) The ω_{iso} precipitates increase effectively the strength and stiffness of β matrix but suppress gradually the activation of deformation mechanisms starting first with martensitic transformation, then dislocation slip and finally 332T. 332T shows unexpected tolerance to the the formation of ω_{iso} precipitates, resulting in a state (ST + 200°C/150s) in which 332T and a very small amount of dislocations slip becomes the deformation mechanism to accommodate tensile strain.

(3) The ω_{iso} strengthen mechanism is due to the increasing CRSS of SIM α'', 332T, and dislocations with the formation of ω_{iso}. The drop of uniform elongation is due to the suppression of SIM α'' and dislocations leading to a decrease of strain-hardening rate. With the further ω_{iso} growth, the alloys become brittle due to the suppression of TRIP/TWIP and dislocation glide deformation mechanisms. By further suppressing

dislocation glide, the twinning operates alone to induce plasticity, i.e. the pure TWIP effect. However, without dislocation glide, the dynamic Hall-Petch effect cannot be effective under such particular circumstance where the dislocation mean free paths are reduced without mobile dislocations.

Acknowledgments:

Fan Sun acknowledges the support of French Agence Nationale de la Recherche (ANR), under grant ANR-21-CE08-0022 (project ISANAMI).

Reference

[1] F. Sun, J.Y. Zhang, M. Marteleur, T. Gloriant, P. Vermaut, D. Laillé, P. Castany, C. Curfs, P.J. Jacques, F. Prima, Investigation of early stage deformation mechanisms in a metastable β titanium alloy showing combined twinning-induced plasticity and transformation-induced plasticity effects, Acta Mater., 61(17) (2013) 6406-6417.

[2] F. Sun, J.Y. Zhang, M. Marteleur, C. Brozek, E.F. Rauch, M. Veron, P. Vermaut, P.J. Jacques, F. Prima, A new titanium alloy with a combination of high strength, high strain hardening and improved ductility, Scr. Mater., 94(0) (2015) 17-20.

[3] J. Gao, P. Castany, T. Gloriant, Complex multi-step martensitic twinning process during plastic deformation of the superelastic Ti-20Zr-3Mo-3Sn alloy, Acta Mater. (2022).

[4] B. Qian, J. Zhang, Y. Fu, F. Sun, Y. Wu, J. Cheng, P. Vermaut, F. Prima, In-situ microstructural investigations of the TRIP-to-TWIP evolution in Ti-Mo-Zr alloys as a function of Zr concentration, J. Mater. Sci. Technol., 1005-0302 (2020).

[5] Y. Danard, G. Martin, L. Lilensten, F. Sun, A. Seret, R. Poulain, S. Mantri, R. Guillou, D. Thiaudière, I. Freiherr von Thüngen, D. Galy, M. Piellard, N. Bozzolo, R. Banerjee, F. Prima, Accommodation mechanisms in strain-transformable titanium alloys, Mater. Sci. Eng. A, 819 (2021) 141437.

[6] J. Gao, A.J. Knowles, D. Guan, W.M. Rainforth, ω phase strengthened 1.2GPa metastable β titanium alloy with high ductility, Scr. Mater., 162 (2019) 77-81.

[7] G.H. Zhao, X.Z. Liang, B. Kim, P.E.J. Rivera-Díaz-del-Castillo, Modelling strengthening mechanisms in beta-type Ti alloys, Mater. Sci. Eng. A, 756 (2019) 156-160.

[8] Y. Gao, Y. Zheng, H. Fraser, Y. Wang, Intrinsic coupling between twinning plasticity and transformation plasticity in metastable β Ti-alloys: A symmetry and pathway analysis, Acta Mater.,196 (2020) 488-504.

[9] F. Sun, J.Y. Zhang, P. Vermaut, D. Choudhuri, T. Alam, S.A. Mantri, P. Svec, T. Gloriant, P.J. Jacques, R. Banerjee, Strengthening strategy for a ductile metastable β-titanium alloy using low-temperature aging, Mater. Res. Lett., 5(8) (2017) 547-553.

[10] B. Qian, L. Lilensten, J. Zhang, M. Yang, F. Sun, P. Vermaut, F. Prima, On the transformation pathways in TRIP/TWIP Ti–12Mo alloy, Mater. Sci. Eng. A, 822 (2021) 141672.

[11] A. Devaraj, S. Nag, R. Srinivasan, R.E.A. Williams, S. Banerjee, R. Banerjee, H.L. Fraser, Experimental evidence of concurrent compositional and structural instabilities leading to ω precipitation in titanium–molybdenum alloys, Acta Mater., 60(2) (2012) 596-609.

[12] T. Li, M. Lai, A. Kostka, S. Salomon, S. Zhang, C. Somsen, M.S. Dargusch, D. Kent, Composition of the nanosized orthorhombic O′ phase and its direct transformation to fine α during ageing in metastable β-Ti alloys, Scr. Mater., 170 (2019) 183-188.

[13] M.J. Lai, T. Li, F.K. Yan, J.S. Li, D. Raabe, Revisiting ω phase embrittlement in metastable β titanium alloys: Role of elemental partitioning, Scr. Mater., 193 (2021) 38-42.

[14] W. Chen, S. Cao, W. Kou, J. Zhang, Y. Wang, Y. Zha, Y. Pan, Q. Hu, Q. Sun, J. Sun, Origin of the ductile-to-brittle transition of metastable β-titanium alloys: Self-hardening of ω-precipitates, Acta Mater., 170 (2019) 187-204.

[15] M.J. Lai, T. Li, D. Raabe, ω phase acts as a switch between dislocation channeling and joint twinning-and transformation-induced plasticity in a metastable β titanium alloy, Acta Mater., 151 (2018) 67-77.

[16] S. Cao, W. Chen, R. Yang, Q.-M. Hu, Origin of the ω-strengthening and embrittlement in β-titanium alloys: Insight from first principles, Phys. Mesomech., 24(5) (2021) 16-25.

[17] S.A. Mantri, F. Sun, D. Choudhuri, T. Alam, B. Gwalani, F. Prima, R. Banerjee, Deformation induced hierarchical twinning coupled with omega transformation in a metastable β-ti alloy, Sci. Rep., 9(1) (2019) 1-8.

[18] F. Sun, D. Laillé, T. Gloriant, Thermal analysis of the ω nanophase transformation from the metastable β Ti–12Mo alloy, J. Therm. Anal. Calorim., 101(1) (2010) 81-88.

[19] R. Salloom, S.A. Mantri, R. Banerjee, S.G. Srinivasan, First principles computation of composition dependent elastic constants of omega in titanium alloys: implications on mechanical behavior, Sci. Rep., 11(1) (2021) 1-21.

[20] J. Nejezchlebová, M. Janovská, P. Sedlák, J. Šmilauerová, J. Stráský, M. Janeček, H. Seiner, Elastic constants of β-Ti15Mo, J. Alloy Compd., 792 (2019) 960-967.

[21] F. Prima, J. Debuigne, M. Boliveau, D. Ansel, Control of omega phase volume fraction precipitated in a beta titanium alloy: Development of an experimental method, J. Mater. Sci. Lett., 19(24) (2000) 2219-2221.

[22] P. Zháňal, P. Harcuba, J. Šmilauerová, J. Stráský, M. Janeček, B. Smola, M. Hájek, Phase Transformations in Ti-15Mo Investigated by in situ Electrical Resistance, Acta Phys. Pol. A, 128(4) (2015).

[23] P. Zháňal, P. Harcuba, M. Hájek, J. Šmilauerová, J. Veselý, M. Janeček, Characterization of Phase Transitions Occurring in Solution Treated Ti-15Mo during Heating by Thermal Expansion and Electrical Resistance Measurements, Trans. Tech. Publ., 2017, pp. 2318-2323.

[24] J. Nejezchlebová, M. Janovská, H. Seiner, P. Sedlák, M. Landa, J. Šmilauerová, J. Stráský, P. Harcuba, M. Janeček, The effect of athermal and isothermal ω phase particles on elasticity of β-Ti single crystals, Acta Mater., 110 (2016) 185-191.

[25] S.A. Mantri, D. Choudhuri, A. Behera, M. Hendrickson, T. Alam, R. Banerjee, Role of isothermal omega phase precipitation on the mechanical behavior of a Ti-Mo-Al-Nb alloy, Mater. Sci. Eng. A, 767 (2019) 138397.

[26] H.Y. Kim, L. Wei, S. Kobayashi, M. Tahara, S. Miyazaki, Nanodomain structure and its effect on abnormal thermal expansion behavior of a Ti–23Nb–2Zr–0.7 Ta–1.2 O alloy, Acta Mater., 61(13) (2013) 4874-4886.

[27] D. De Fontaine, N.E. Paton, J.C. Williams, The omega phase transformation in titanium alloys as an example of displacement controlled reactions, Acta Metall., 19(11) (1971) 1153-1162.

[28] J. C. Williams, B. S. Hickman, and H. L. Marcus, The effect of omega phase on the mechanical properties of titanium alloys, Metall. Trans., 2(7)(1971) 1913-1919.

[29] S. A. Mantri, D. Choudhuri, T. Alam, V. Ageh, F. Sun, F. Prima, R. Banerjee, Change in the deformation mode resulting from beta-omega compositional partitioning in a Ti-Mo alloy: Room versus elevated temperature, Scr. Mater., 130 (2017) 69-73.

[30] F. De Geuser, W. Lefebvre, D. Blavette, 3D atom probe study of solute atoms clustering during natural ageing and pre-ageing of an Al-Mg-Si alloy, Philos. Mag. Lett., 86(04) (2006) 227-234.

[31] J. M. Hyde, E. A. Marquis, K.B. Wilford, T.J. Williams, A sensitivity analysis of the maximum separation method for the characterisation of solute clusters, Ultramicroscopy 111(6) (2011) 440-447.

[32] L. T. Stephenson, M. P. Moody, P. V. Liddicoat, S.P. Ringer, New techniques for the analysis of fine-scaled clustering phenomena within atom probe tomography (APT) data. Microscopy and Microanalysis, 13(6) (2007), 448-463.

[33] B. Qian, M. Yang, L. Lilensten, P. Vermaut, F. Sun, F. Prima, In-situ observations of a hierarchical twinning–detwinning process in stress-induced α″-martensite of Ti-12Mo alloy, Res. Lett., 10(2), 45-51.

[34] M. Li, X. Min, Origin of ω-phase formation in metastable β-type Ti-Mo alloys: cluster structure and stacking fault, Sci. Rep., 10(5) (2020) 1–15.

[35] P. Kwasniak, F. Sun, S. Mantri, R. Banerjee, F. Prima, Polymorphic nature of {332}<113> twinning mode in BCC alloys, Mater. Res. Lett., 10 (2022) 334-342.

[36] E. Bertrand, P. Castany, I. Péron, T. Gloriant, Twinning system selection in a metastable β-titanium alloy by Schmid factor analysis, Scr. Mater., 64(12) (2011): 110-113.

[37] P. Castany, Y. Yang, E. Bertrand, T. Gloriant, Reversion of a parent {130}<310>α″ martensitic twinning system at the origin of {332}<113>β twins observed in metastable β titanium alloys. Phys. Rev.

Lett., 117(24), 245501.

Supplementary materials

Table S1 Mechanical properties of Ti-12Mo after different strengthening treatments from as-cold-rolled state.

Alloy states	ST (coarse grain)[10]	ST (fine grain)	ST + 200°C/60s	ST + 200°C/150s	ST + 200°C/300s
Thermal treatment history	900°C/1.8ks WQ*	900°C/60s WQ	ST (fine grain) + 200°C/60s	ST (fine grain) + 200°C/150s	ST (fine grain) + 200°C/300s
Yielding strength, σ_s (MPa)	478±24	659±33	865±43	990±48	1048±52
Young's modulus, E *(GPa)*	82±4	76±4	110±6	115±6	140±7
Ultimate tensile strength σ_{UTS} (MPa)	975±4	1093±55	1141±57	990±48	1048±52
Uniform elongation	39±5%	29±5%	33±5%	3.3±1%	<1%
Average Grain size (μm)	100±5	20±2	20±2	20±2	20±2

***WQ: water-quenching**

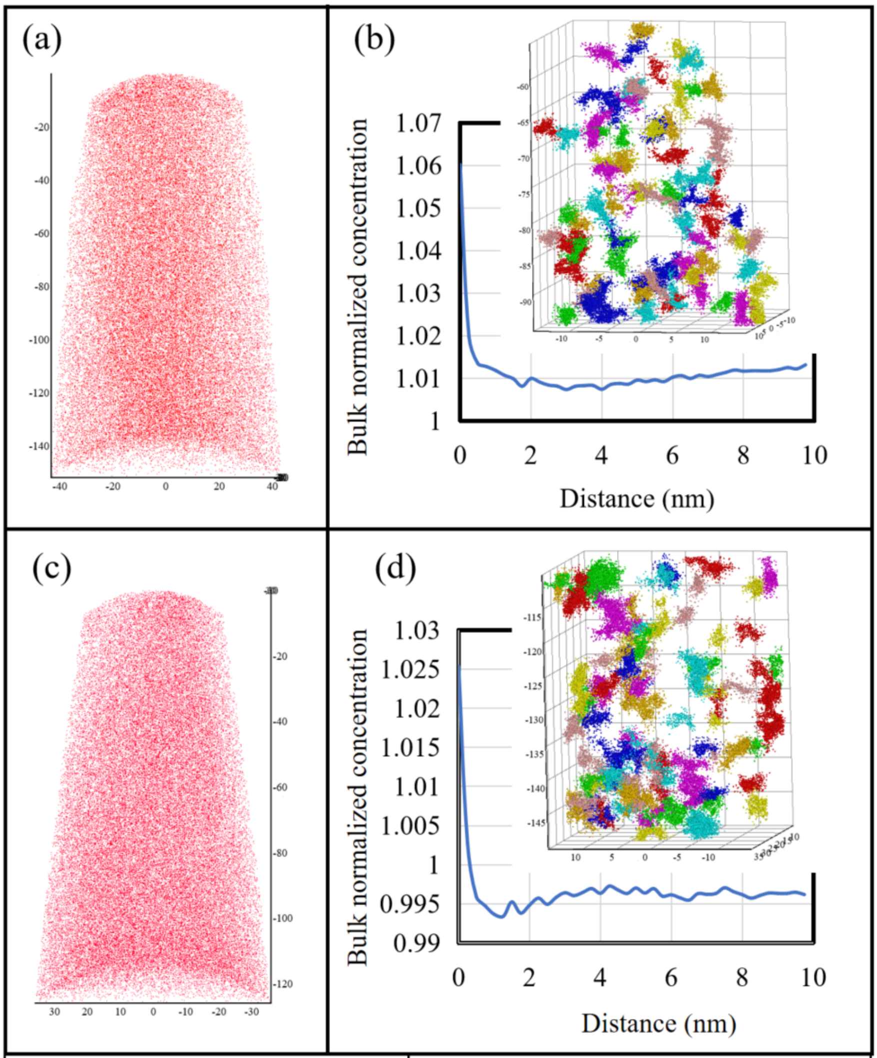

(e)

Cluster analysis ST + 200℃/60s sample		Cluster analysis ST + 200℃/150s sample	
Ion	Mo	Ion	Mo
Volume fraction	12.30	Volume fraction	16.00
Average radius(nm)	2.54	Average radius(nm)	2.80
Mo at.%	39.91	Mo at.%	38.36

Figure S1 Atom probe temography (APT) results from (a-b) the ST + 200°C/60s sample and (c-d) the ST + 200°C/150s sample: (a and c) raw ion map of Mo and (b and d) radial distribution function maps of Mo ions; (e) cluster analysis from the ST + 200°C/60s sample and the ST + 200°C/150s

sample.